METALLURGICAL RISK FACTORS IN GRADE 91 STEEL

Sharhid Jabar, Geoff D West
WMG, University of Warwick, Coventry, UK.

Barbara Shollock
Kings College, London, UK.

John Siefert
Electric Power Research Institute, Charlotte, NC, USA.

ABSTRACT

Modified 9Cr-1Mo steel (ASTM Gr.91) is widely used in components of fossil fueled power plants around the world today. This grade of steel has however been shown to exhibit significant variations in creep life and creep ductility, which has led to premature in-service failures. The aim of this work is to define the metallurgical risk factors that lead to this variation in performance. To achieve this, a set of creep test samples that represent a wide range in this variation of creep behavior in this steel grade have been studied in detail. As a first stage in this characterization the macro-scale chemical homogeneity of the materials were mapped using micro-XRF. Understanding the segregation behavior also allows quantification of microstructural parameters in both segregated and non-segregated areas enabling the variations to be determined. For example this showed a significant increase in the number per unit area of Laves phase particles in high compared with low Mo content areas. To study the effect of MX particles on segregation a methodology combining SEM and TEM was employed. This involved chemically mapping the larger V containing particles using EDS in the SEM in segregated and unsegregated areas and then comparing the results to site-specific TEM analysis. This analysis showed that although the average size of the V containing samples is in the expected 0-50 nm size range, these particles in some samples had a wide size distribution range, which significantly overlaps with the $M_{23}C_6$ size distribution range. This together with the segregation characteristics has important implications for determining meaningful quantitative microstructural data from these microstructurally complex materials.

INTRODUCTION

Grade 91 steel was introduced in the 1980's [1], its application became widespread amongst the power generation industry in years to follow thanks to a good compromise of cost and performance [2]. The long term performance of creep strength enhanced ferritic 9-12 Cr% steels has been well documented and related to the precipitation of intermetallic phases during creep (Z and Laves phase) [3,4]. The wide-ranging processing parameters and permissible composition of the Gr.91 ASTM code [5] has meant heat to heat variations in P91 have produced variable creep properties with respect to time to rupture and ductility compared to other similar grades. This led to the formation of an EPRI guideline for P91 steel [6], which encourages the limitation of many 'tramp' elements (from recycled scrap) that are originally neglected by ASTM standards. Furthermore, variations in heat treatment temperatures and mechanical testing requirements has meant a lot of P91 components have not been fit for purpose under demanding creep conditions. This has resulted in a number of catastrophic failures that were initially attributed to a N:Al ratio that resulted in AlN formation that subsequently limited the populations of precipitation strengthening VN particles [7-8]. However, more recent work has shown that the variation in

creep strength is more complicated and likely linked to a combination of the thermal processing schedule of the steel, the presence of tramp elements and the population characteristics of microstructural features onto which cavities can nucleate (such as inclusions) [11].

The normalizing and tempering heat treatments are important to homogenize the chemical composition of the steel and produce a tempered martensitic microstructure. In such high alloy steel however, the normalizing times are insufficient to completely homogenize the chemical composition. The impact of chemical segregation on the precipitation of phases in Gr.91 steel has yet to be studied in detail, however recently it has been associated with a loss in creep rupture strength [9]. The segregation behavior of a ZG12Cr9Mo1Co1NiVNbNB ferritic steel has recently been reported [12]. It showed a high enrichment in Cr, Mo, and Mn during the end of the solidification process of a cast due to inhomogeneous cooling through its thickness. This segregation also caused a hardness variation in the cast, with the parts near chills (fast cooling) having a more consistent hardness due to the suppression of segregation [12]. Furthermore, a link between the degree of chromium segregation in a T91 (Tubular Gr.91) steel and creep rupture life has been recognized, showing a greater variation of chromium concentration through the thickness of the tube correlating with a loss of creep strength [5]. This is because it is recognized that these segregated regions may be the location of the notoriously harmful Z-phase [10] and other pre-existing phases such as inclusions and NbC particles [12].

The motivation of this work is to explore the effect of segregation on 2nd phase particles of 2 ex-service steels produced using different procedures through the analysis of double notched creep tested bars. Comparing the size distributions of various precipitates in the head section (reduced stress) to the failed gauge section.

MATERIALS AND METHEDOLOGY

The materials used in this work were from the ex-service P91 header shown in Fig.1A, which had failed after 79,000 hours of service, although its design life was expected to be double this [8]. Failed double notch creep bars (Fig.1B-C) from the parent metal of both B2 and TP1 sections of the header were provided for analysis. The creep test conditions are detailed in Tab.1. The composition of the two steels was measured by Dirats Laboratories using OES-ICP and is shown in Tab.2. Samples were sectioned along the axis of the bars so that the microstructure in specific

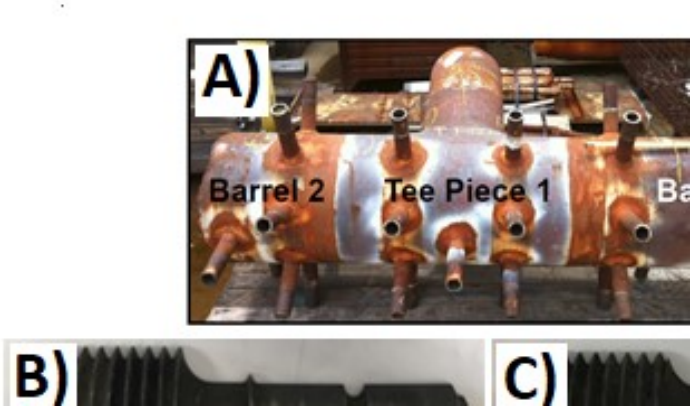

Figure 1: Photograph of the header from which parent B2 and TP1 material was taken (A). Photographs of the failed double notched creep test bars for sample B2 (B) and TP1 (C).

Material ID	Type of Test	Test Conditions			ROA (%)	OD/ID of gauge (mm)
		Temp. (°C)	Stress (MPa)	Time to Failure (hours)		
B2	Type 1 Notch Bar	625	100	1,408	N/A	10/7
			~50*	~1.5% life fraction		
TP1			100	6,714		
			~50*	~1.5% life fraction		

Table 1: Creep test conditions and performance of B2 and TP1

Sample	Weight % composition (Fe = balance)												
	Al	Cr	Mn	Mo	Nb	Ni	Si	V	C	S	N	Co	P
B2	0.039	8.774	0.43	0.92	0.067	0.15	0.412	0.224	0.079	0.0086	0.045	0.017	0.009
TP1	0.014	8.232	0.43	0.91	0.058	0.24	0.382	0.214	0.077	0.0019	0.046	0.012	0.017

Table 2: Chemical compositions of B2 and TP1

regions (e.g. head, gauge and notch section) could be determined. Samples were prepared using standard metallographical procedures with a final step of 0.02 µm MasterPrep alumina suspension from Buehler.

The macro-scale homogeneity of the two samples was assessed using a Bruker M4 Tornado micro-X-Ray Fluorescence (µ-XRF) system equipped with two 30 mm^2 EDS detectors. Maps were collected with a step size of 20 µm at 50 kV and using a current of 600 mA in vacuum. An AlTi 100/25 sandwich filter was used to minimize diffraction peaks and quant data was extracted from the intensity maps. Quantitative data was produced by performing an automated background subtraction from all spectra in the map and using inbuilt quantification algorithms within the Bruker software. Areas of interest defined by the µ-XRF were studied in more detail using a JEOL 7800F Field Emission Gun Scanning Electron Microscope (FEG-SEM) equipped with a solid-state Backscattered Electron (BSE) detector and an Oxford Instruments ultimax 100 mm^2 Energy Dispersive Spectroscopy (EDS) detector. Large area EDS maps were collected at 10 kV for extended time periods (12 hours) with a current of around 3 nA that maximized collection efficiency of the detector and provides the highest possible sensitivity in the EDS derived chemical distribution maps. Higher magnification maps were also collected to show the particle distributions, these were collected with the same parameters only with shorter acquisition times. BSE SEM images were collected, also at 10 kV, in defined locations to measure the number per unit area of second phase particles. Five images and maps were collected from each area type and the images were processed using Image J. Site specific Transmission Electron Microscopy (TEM) samples from defined planar surface areas in B2 were prepared using a FEI Versa dual beam Focused Ion Beam (FIB)-SEM. An FEI Talos F200X Field Emission Gun (Scanning) Transmission Electron Microscope (FEG-TEM) equipped with a Super X EDS system was used to analyze the FIB prepared TEM samples. EDS maps with statistically high counts were collected so that the second phase particles in the analyzed volume could be studied.

RESULTS AND DISCUSSION

XRF and EDS Segregation

The macro-scale chemical homogeneity of the key alloying elements (Cr, V, Nb, Mo) of B2 and TP1 are displayed in the µ-XRF derived chemical distribution maps in Figs.2 and 3. These elements are also the main components of $M_{23}C_6$, MX precipitates and Laves phase. The µ-XRF maps were collected from the head sections, threaded regions were included in the maps to act as reference points for subsequent SEM and TEM experiments. Quantified max and min (high and low) compositions are given in Tab.3, areas were acquired using a selected area (50 µm x 100 µm).

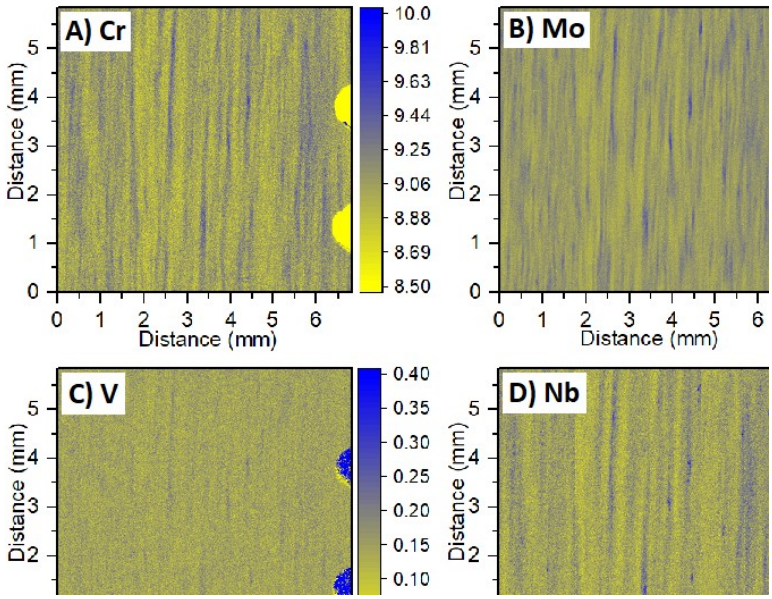

Figure 2: µ-XRF derived quantitative chemical distribution maps for Cr (A), Mo (B), V (C) and Nb (D) collected in the head region of B2. (Compositions in Wt.%).

From Fig.2 the segregation in B2 has a banded structure due to the elongation processes used during production. In TP1 meanwhile the segregation characteristics are very different with segregated regions forming 'clouds'. These differences in segregation can be attributed to the different forming methods; B2 is a pierced pipe and TP1 is a forging pipe. All the key alloying elements can be seen to segregate in similar manner. This is shown quantitatively in Tab.3 where the composition of maximum and minimum regions are compared. It can be see that TP1 has a larger composition range in all elements. For both samples it can be seen that the percentage change in Mo between a 'high' and 'low' area is greater than for Cr. This can be attributed to the slower diffusion times of the large Mo atom making it more difficult to homogenize than Cr. To examine the segregated characteristics in more detail areas where the Cr content is above 2% of the average value for Cr and above 5% of the average value of Mo are compared for both samples in Fig.4.

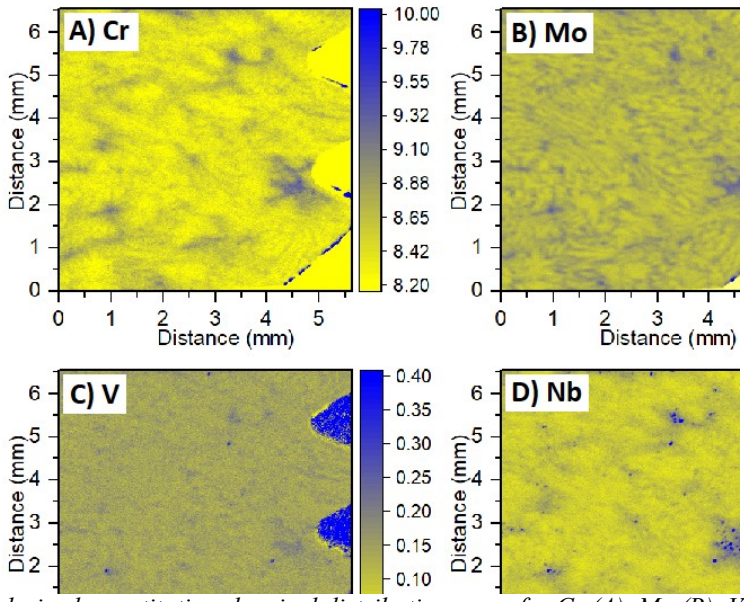

Figure 3: µ-XRF derived quantitative chemical distribution maps for Cr (A), Mo (B), V (C) and Nb (D) collected in the head region of B2. (Compositions in Wt.%).

Sample	**Cr**		**V**		**Nb**		**Mo**	
Conc. Wt(%)	High	Low	High	Low	High	Low	High	Low
B2	9.35	8.97	0.19	0.16	0.07	0.05	0.94	0.76
TP1	9.21	8.34	0.21	0.16	0.10	0.05	1.08	0.78

Table 3: Max and Min chemical compositions of B2 and TP1 using XRF

These maps clearly show the higher percentage segregation of Mo compared with Cr and the co-segregation of both elements. In order to assess the effect of segregation on microstructural features such as precipitated particles, it is desirable to observe the segregation directly in the SEM. To do this EDS maps were acquired for long durations (approx. 10 hours) with high count rates (>150 k cps output). The location of the large area EDS maps for both samples were selected based on the µ-XRF maps shown in Figs.2 and 3 to ensure a segregated region of interest was included in the map. Figure 5 shows the Cr and V distribution maps from both samples and Tab.4 provides quantified compositions from key regions. It can be seen that the composition difference within a sample is lower than was measured with µ-XRF, this is likely to be due to a combination of the reduced sampling area and interaction volume of EDS compared with µ-XRF. This is because since only a small portion of a segregated band can be detected within a single EDS map it is unlikely that features in the map represent true maximum and minimum composition values.

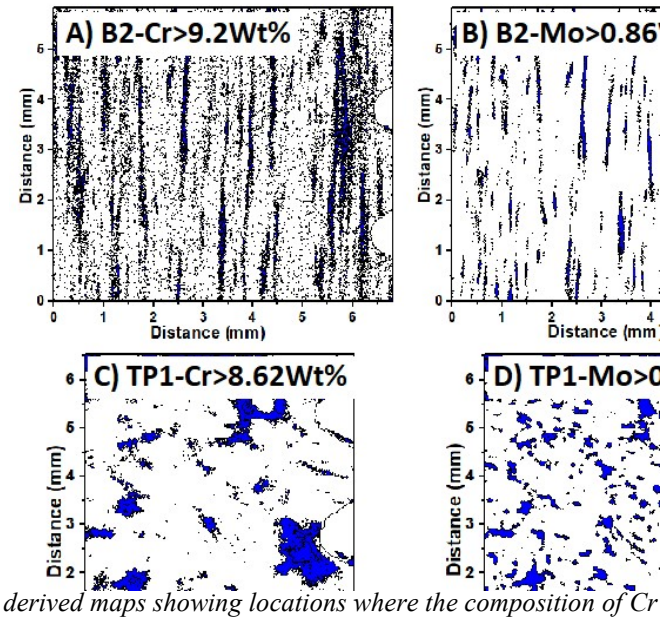

Figure 4: µ-XRF derived maps showing locations where the composition of Cr and Mo is 2% and 5% above the average composition respectively for B2 (A-B) and TP1 (C-D).

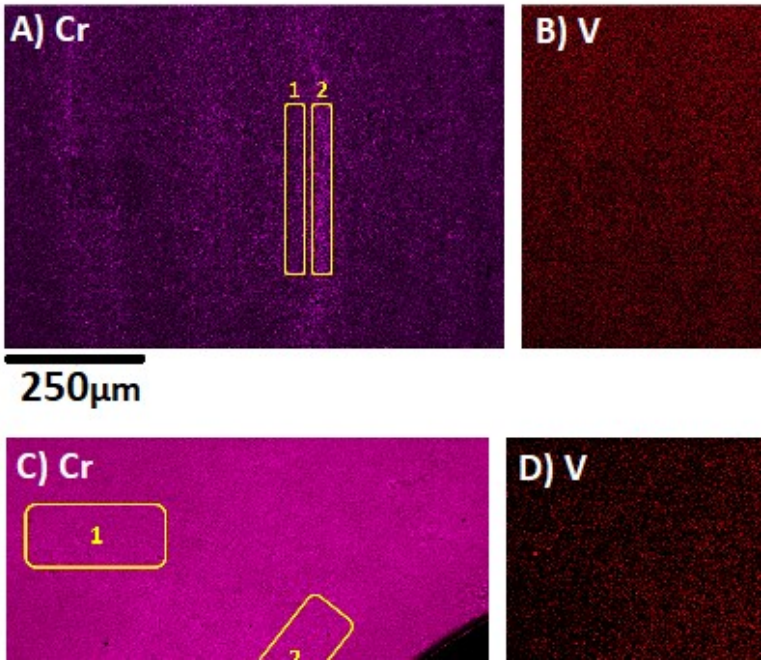

Figure 5: EDS in SEM derived chemical distribution maps for Cr and V for B2 (A-B) and TP1 (C-D). Area from where compositional data were extracted are annotated.

Spectra	Al	Si	V	Cr	Mn	Mo	Ni	Nb
1A-B2 Low	0.05	0.45	0.24	8.93	0.49	0.99	0.22	0.05
2A-B2 High	0.06	0.47	0.29	9.32	0.47	1.25	0.04	0.06
1C-TP1 Low	-	0.53	0.22	8.27	0.21	0.92	0.53	-
2C-TP1 High	-	0.51	0.23	8.50	0.23	0.98	0.55	0.04

Table 4: Max and Min chemical compositions of B2 and TP1 using EDS in SEM from areas

Effect of segregation on second phases

Figure 6 shows a comparison of a BSE image collected in an area with lower than average Cr/Mo content with an area with higher than average Cr/Mo for sample B2. The bright particles in the images are Laves phase particles and the dark particles are AlN. The areas were defined by XRF and then EDS analysis as was shown in Figs.2, 3 and 5. Figure 7 shows a comparison of the number per unit area of Laves phase particles as a function of size in sample B2 and TP1 in segregated and non-segregated regions and in the head and gauge sections of the samples. The shapes of all size distribution curves are similar, and there is a clear and significant increase in the number of Laves phase particles in high Mo content areas compared with low Mo content areas, for both regions of both samples. The increase in Laves phase particle number between the high and low Mo content regions in the head section of the TP1 samples is much smaller than in the other samples/area, however this is consistent with the much smaller difference in Mo content between these regions as shown in Tab.3. The number of Laves phase particles per unit area is also much higher in the head sections than the gauge sections for both samples. Although this difference is large (e.g. almost double for TP1 in high Mo areas), if a high Mo area in the gauge is compared with a low Mo area in the head for the B2 sample the results are comparable. This shows that average Laves particle characteristics can only be achieved if images are collected from areas with a representative distribution of segregation characteristics. This also asks the question whether it is the average number per unit area that is the key parameter or whether the maximum number per unit area would be a more appropriate.

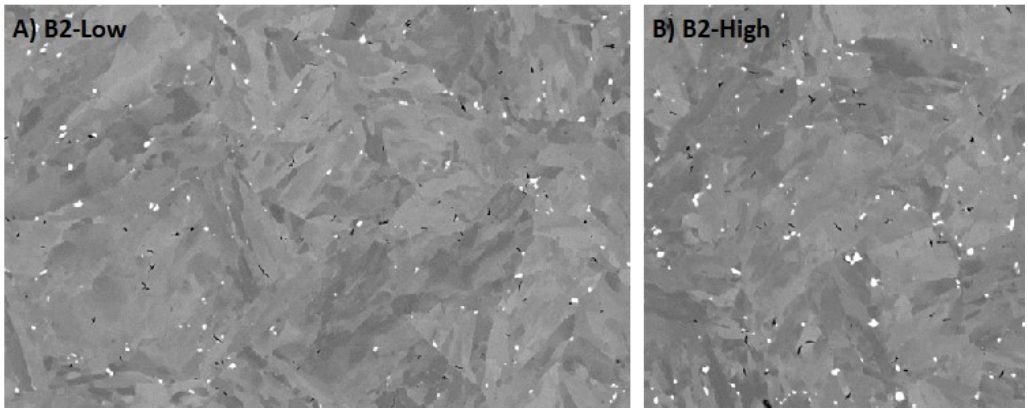

Figure 6: BSE images of a low Mo/Cr region (A) and a high Mo/Cr region (B) in the head section of the B2 sample

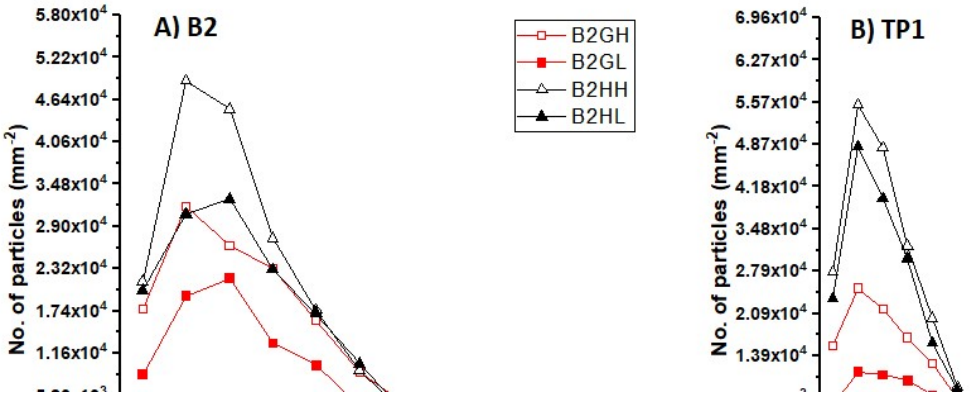

Figure 7: Graphs showing the size distribution of Laves phase particles in high and low Mo containing regions in the head and Gauge sections for B2 (A) and TP1 (B). (GH = gauge high, GL = gauge low, HH = Head High, HL = Head Low)

Sample	Amount of particles per mm^2			
	Gauge		Head	
	High	Low	High	Low
B2	135,000	81,700	177,100	141,100
TP1	108,400	52,600	200,200	173,000

Table 5: Number of laves phase particles per unit area in high and low Mo/Cr regions for B2 and TP1 in the head and gauge regions.

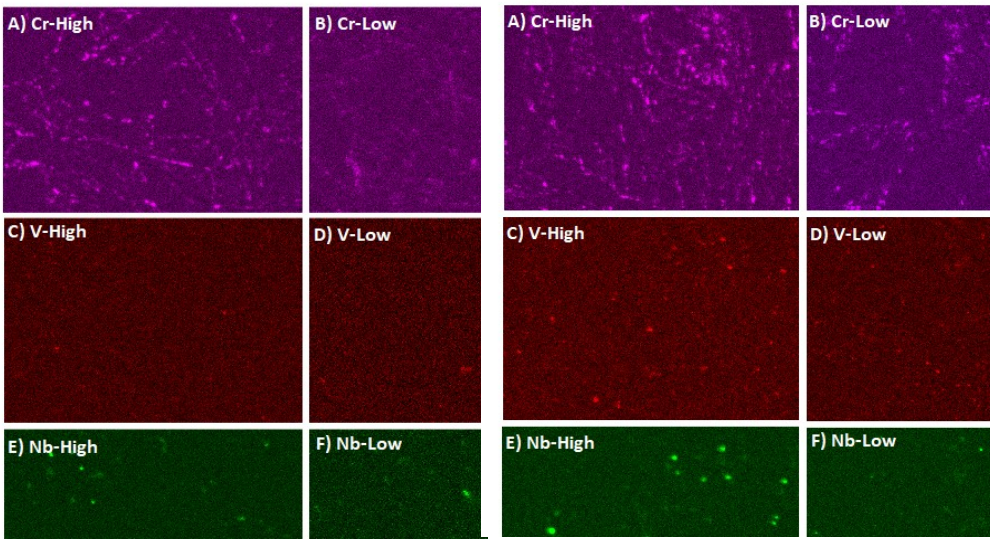

Figure 8: EDS derived chemical distribution maps from head sections in B2 (left) and TP1 (right).

The effect of Cr/V segregation on the characteristics of the $M_{23}C_6$ and MX population distributions was also investigated. Figure 8 shows EDS derived chemical distribution maps for Cr, V and Nb for B2 and the TP1 areas in 'high' and 'low' Cr areas. Although there are apparent differences between the maps shown, the difference between the set of maps collected are less clear. It is also noteworthy that the V chemical distribution map clearly showed the presence of V-rich (MX) particles. Although the EDS maps were collected at 10 kV to have a sufficient energy range whilst achieving the best spatial resolution possible, the spatial resolution is insufficient for robust size analysis. To achieve an improvement in spatial resolution TEM samples were prepared from planar sections of high and low Cr/V areas in the head of the B2 sample. Figure 9 shows chemical distribution maps collected using EDS in STEM. Diffraction analysis showed that the Cr-rich particles are $M_{23}c_6$ and the V-rich particles are MX. The size distribution of the particles collected in this map are plotted in Fig.10. This shows that there is no clear differences in the distribution characteristics of MX of $M_{23}C_6$ particles in 'low' and 'high' Cr/V areas at the length scale used. This can be attributed to a combination of the relatively small differences in chemistry between the areas and more importantly the very limited area that could be analyzed in this way.

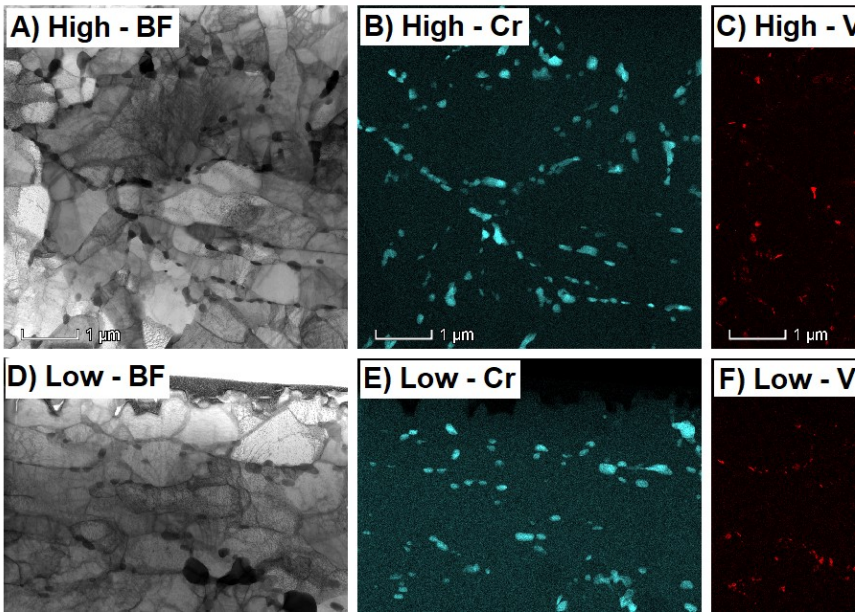

Figure 9: BF STEM and corresponding chemical distribution maps from high and low Cr regions in sample B2

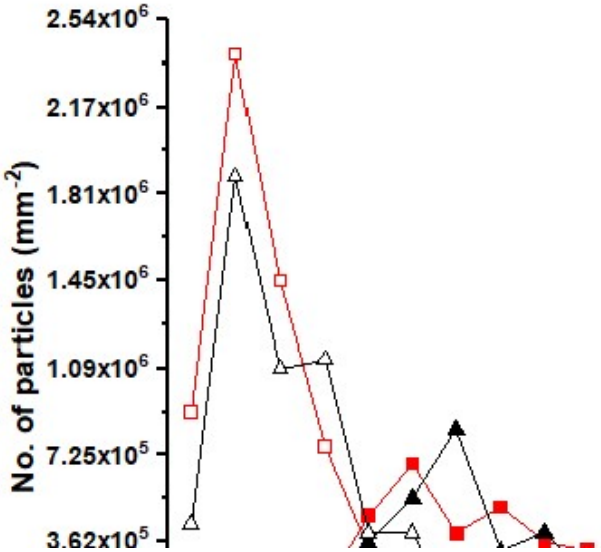

Figure 10: Size distributions of MX and $M_{23}C_6$ precipitates in B2 from the EDS data shown in Fig.9.

CONCLUSIONS

- Segregation effects in the P91 can have important effects on the number per unit area of second phase particles. This is particularly important for Laves phase as the level of segregation is higher for heavy elements such as Mo than lighter elements such as Cr.
- The segregation characteristics of the steel should be understood before undertaking quantitative analysis of microstructural features. The segregation characteristics can be very different depending on the thermal mechanical processing of the component; in this work the segregation behavior of a pierced pipe is shown to be very different to that of a forged pipe.
- Cr/V segregation has a less clear effect on the particle population characteristics of $M_{23}C_6$/MX.
- An overlap in the size distribution of the $M_{23}C_6$ and MX particles means that a chemical based process is required to isolate the individual populations.
- Analysis of the size of the MX-type particles shows that the largest particles in the population are >100 nm. The number of the large particles per unit area is likely to be a key parameter in the creep strength as large particles suggest a decrease in the number density of the particles.

ACKNOWLEDGMENTS

The Electric Power Research Institute are acknowledged for funding this project on metallurgical risk factors in 9Cr steel. The technical assistance from Dr. Tapasvi Lolla (EPRI) and Dr. Sabrina Yan (WMG) was greatly appreciated.

REFERENCES

[1] J. R. DiStefano, V. K. Sikka, J. J. Blass, C. R. Brinkman, J. M. Corum, J. A. Horak, R. L. Huddleston, J. F. King, R. W. McClung, and W. K. Sartory. Summary of modified 9Cr-1Mo steel development program, 1975-1985. No. ORNL-6303. Oak Ridge National Lab.(ORNL), Oak Ridge, TN (United States), 1986.

[2] F. Masuyama. "New developments in steels for power generation boilers." Advanced Heat Resistant Steel for Power Generation (1998): 33-48.

[3] J. Hald. "Microstructure and long-term creep properties of 9–12% Cr steels." International Journal of Pressure Vessels and Piping 85, no. 1-2 (2008): 30-37.

[4] X. Z, Zhang, Wu X. J, Liu. R, J. Liu, and M. X. Yao. "Influence of Laves phase on creep strength of modified 9Cr-1Mo steel." Materials Science and Engineering: A 706 (2017): 279-286.

[5] A335/A335M-10b, 2015. Standard specification for seamless ferritic alloy–steel pipe for high temperature service, ASTM International, West Conshohocken, PA, USA.

[6] J. D. Parker, K. Coleman, J. Henry, W. Liu, and G. Zhou. "Guidelines and Specifications for High-Reliability Fossil Power Plants: Best Practice Guideline for Manufacturing and Construction of Grade 91 Steel Components 1023199." Electric Power Research Institute, California (2011).

[7] Brett, S. J., D. J. Allen, and J. Pacey. "Failure of a modified 9Cr header endplate." Case Histories on Integrity and Failures in Industry, V. Bicego, A. Nitta, JWH Price, and R. Viswanathan, eds (1999): 837-884.

[8] J. D. Parker, and Brett. S. "Creep performance of a grade 91 header." International Journal of Pressure Vessels and Piping 111 (2013): 82-88.

[9] K. Kimura and K. Sawada. "Influence of chemical composition and materials processing on creep strength of Grade 91 steels." 4th International ECCC Conference. Dusseldorf, Germany. 10-14 Sept 2017.

[10] K. Sawada, K. Sekido, H. Kushima and K. Kimura. "Microstructural degradation during long-term creep in 9-12%Cr steels." 4th International ECCC Conference. Dusseldorf, Germany. 10-14 Sept 2017.

[11] J. A. Siefert, R. C. Thomson, and J. D. Parker. "Microstructure Features Contributing to Heat Affected Zone Damage in Grade 91 Steel Feature Type Cross-Weld Tests." In ASME 2018 Symposium on Elevated Temperature Application of Materials for Fossil, Nuclear, and Petrochemical Industries, pp. V001T03A002-V001T03A002. American Society of Mechanical Engineers, 2018.

[12] B. Wang, H. Zhong, X. Li, X. Wang, T. Wu, Q. Liu and Q. Zhai. "Thermal Simulation Study on the Solidification Structure and Segregation of a Heavy Heat-Resistant Steel Casting." Metals 9, no. 2 (2019): 249.